



**Development of Magnesium Oxide-Silver Hybrid
Nanocatalysts for Synergistic Carbon Dioxide Activation to
Afford Esters and Heterocycles at Ambient Pressure**

| | |
|-------------------------------|--|
| Journal: | <i>Green Chemistry</i> |
| Manuscript ID | GC-ART-11-2019-004040.R1 |
| Article Type: | Paper |
| Date Submitted by the Author: | 02-Mar-2020 |
| Complete List of Authors: | Gulati, Upasana; Indiana University Bloomington, Chemistry Ummadisetti, Chinnarajesh; Indiana University Bloomington, Chemistry Rawat, Diwan; University of Delhi, Department of Chemistry Zaleski, Jeff; Indiana University, Department of Chemistry |
| | |

ARTICLE

Development of Magnesium Oxide-Silver Hybrid Nanocatalysts for Synergistic Carbon Dioxide Activation to Afford Esters and Heterocycles at Ambient Pressure

Received 00th January 20xx,
Accepted 00th January 20xx

DOI: 10.1039/x0xx00000x

Upasana Gulati,^{a,b†} U. Chinna Rajesh,^{a†} Diwan S. Rawat^{b*} and Jeffrey M. Zaleski^{a*}

Multi-metallic hybrid nanocatalysts consisting of a porous metal oxide host and metal satellite guests serve as a scaffold for multi-step transformations of divergent and energy-challenging substrates. Here we have developed a 3D porous MgO framework (Lewis basic host) with Ag⁰ nanoparticles (noble metal guest) for ambient pressure activation and insertion of CO₂ into unsaturated alkyne substrates. The hybrid MgO@Ag-x (x = 2, 5, 7, 8 at % Ag) catalysts are synthesized by impregnating Ag⁺ ions in porous MgO cubes followed by reduction using NaBH₄. Morphological (SEM, TEM, EDX mapping) and structural (PXRD, XPS) characterization reveal that the micron-sized hybrid cubes derive from self-assembly of ~100 nm (edge length) MgO cubes decorated with ~5 to 25 nm Ag⁰ NPs. Detailed XPS analysis illustrates Ag⁰ is present in two forms, <10 nm NPs and ~25 nm aggregates. The MgO@Ag-7 catalyst is effective for inserting CO₂ into aryl alkynes followed by S_N2 coupling with allylic chlorides to afford a wide range of ester and lactone heterocycles in excellent yields (61-93%) and with low E-factor (2.8). The proposed mechanism suggests a CO₂ capture and substrate assembly role for 3D porous MgO while Ag⁰ performs the key activation of alkyne and CO₂ insertion steps. The catalyst is recyclable (5x) with no significant loss of product yield. Overall, these results demonstrate viable approaches to hybrid catalyst development for challenging conversions such as CO₂ utilization in a green and sustainable manner.

Introduction

Feedstock utilization of CO₂, a major component of flue gas responsible for global warming, is an environmentally benign approach to chemical transformations of scale.¹⁻³ It is non-toxic, abundant, and a cost-effective one-carbon building block for fuels and industrially-relevant chemical production.⁴ The conventional and non-catalytic industrial usage of CO₂ feedstock includes the effective syntheses of urea, salicylic acid, and carbonates of groups 1 and 2 elements.⁵ However, all these processes involve high pressure and temperature conditions due to the enhanced kinetic and thermodynamic stability of the fully oxidized CO₂ molecule.^{3, 4} Therefore, the development of catalysts for efficient CO₂ utilization mandates reducing the activation energy of the chemical reaction.⁴ In addition to effective CO₂ management, the development of green chemical methodologies can have significant environmental benefits.^{4, 6, 7} Economic advantages also derive from quantification and minimization of waste produced per

unit product (E-factor).^{8, 9} Hence, a sustainable, green chemical approach must be energy efficient and produce less waste as its disposal requires more resources to manage.

There are various reports of homogeneous transition metal (Fe, Ni, Cu, Ag, Pd) catalysts for activation of small molecule (CO₂) and unsaturated organic functionalities (olefin, alkyne) to afford CO₂ inserted, value-added chemicals.¹⁰⁻¹⁷ For example, Ni⁰ and Fe⁰ catalysts have been developed for carboxylation of olefins (Csp²-H) by CO₂ insertion to produce acrylic acid.¹⁰⁻¹² Additionally, Ag⁺ and Cu⁺ catalysts have also been shown to activate alkynes (Csp-H) followed by CO₂ insertion to afford propiolic acid derivatives.¹⁵⁻¹⁸ While effective, these homogeneous catalysts suffer from corrosion, catalyst leaching, low recyclability, and often these processes require high pressures of CO₂.¹⁹

The development of 3D porous nanomaterials capable of CO₂ capture, decorated with transition metal satellites for active catalysis, can overcome these limitations in a green and sustainable manner.¹⁹⁻²³ The porous nanomaterials having Lewis basic/acidic sites and large surface area like metal organic frameworks (MOFs), covalent organic frameworks (COFs), porous organic polymers, hetero-atom doped porous carbon and porous metal oxides are capable of capturing CO₂ at ambient to high pressure conditions.¹⁹ The hybrid composition of these porous materials with Ag⁰ satellites such as Ag@MIL,²⁰ ZIF@Ag,²⁴ Co-MOF@Ag,²² poly-NHC@Ag,²⁵ CeO₂@Ag²³ provides a gateway to myriad of CO₂ inserted value added synthons. However, the catalytic systems for

^a Department of Chemistry, Indiana University, Bloomington, Indiana 47405, United States. E-mail: zaleski@indiana.edu

^b Department of Chemistry, University of Delhi, Delhi-110007, India. E-mail: dsrawat@chemistry.du.ac.in

[†] These authors contributed equally to the work.

Electronic Supplementary Information (ESI) available: [Experimental section, Material characterization, E-factor table, Organic compounds data and spectra]. See DOI: 10.1039/x0xx00000x

activation of multiple substrates like alkynes and allylic chlorides for CO₂ insertion continues to require high pressure conditions.^{15, 17, 23} Thus, there is considerable need for the development of heterogeneous catalysts that have greater adsorptive interactions with CO₂ and are capable of activating multiple substrates for fine chemical generation.

Recently, Lewis basic, porous MgO has been shown to have high adsorption capacity for CO₂ at low-coordinate (111) facets rich with O²⁻ functionality,²⁶ but its potential to facilitate CO₂ insertion into energetically challenging substrates is under explored. In general, the fixation process requires a catalyst with Lewis acid/basic sites that take advantage of the net charges on oxygen and carbon to bind CO₂ in concert with direct attack at carbon by a nucleophilic substrate to reduce and form a new C-C bond. The enzyme Rubisco accomplishes this same task at Mg²⁺ by compromising the ribulose biphosphate substrate via deprotonation, leading to subsequent nucleophilic attack on CO₂ by an adjacent and unsaturated carbon.²⁷ Since porous MgO can bind CO₂ efficiently but not perform the activation of stable organic substrates directly, development of a catalyst component that can serve to activate carbon frameworks forming the key CO₂ attacking nucleophile is critical to enhancing substrate scope.

Toward these goals, we report the synthesis of 3D porous MgO frameworks containing dual Lewis acid/basic sites with embedded Ag NPs for insertion of ambient pressure CO₂ into organic substrates. The novel MgO@Ag hybrid catalyst is employed to incorporate CO₂ into alkynes followed by S_N2 coupling with allylic chlorides to afford esters and lactone heterocycles. The catalytic system is effective at ambient pressure of CO₂, recyclable, and exhibits a low E-factor demonstrating its importance to green and sustainable solutions for CO₂ fixation.

Results and discussion

MgO@Ag hybrid nanocatalyst synthesis and structural morphology. Development of three dimensional (3D) porous MgO (host) embedded with Ag⁰ nanoparticles (guest) possess unique advantages in the catalysis arena. The present study shows the facile synthesis of 3D porous MgO@Ag-x (where x = 2, 5, 7, 8 at % Ag) hybrid nanocatalysts by a three-step process (Figure 1). Initially, the 3D porous MgO cubes are obtained by the calcination of MgC₂O₄·2H₂O precursor at 800 °C for 3 h. The impregnation of Ag⁺ ions on the surface and inside the pores of MgO cubes was achieved by aging various quantities of AgOAc with MgO cubes in ethanol at ambient temperature. Finally, the reduction of Ag⁺ ions to Ag⁰ nanoparticles is achieved by using NaBH₄ to produce MgO@Ag-x hybrid 3D porous structures. The surface morphology (SEM) and elemental distribution (SEM-EDX) of the MgO@Ag-x hybrid materials (MgO@Ag-2, MgO@Ag-5, MgO@Ag-7 and MgO@Ag-8) show micron sized (~1-2 μm) porous MgO cubes decorated uniformly with Ag⁰ nano satellites with a systematic increase in density upon increasing concentration of silver precursor (0.07 to 0.30 mmol, Figure S1). When the impregnation and reduction steps are performed in water, the morphology and

structure of the 3D porous MgO cubes changes into non-porous Mg(OH)₂ flakes (Figures S2 and S3).

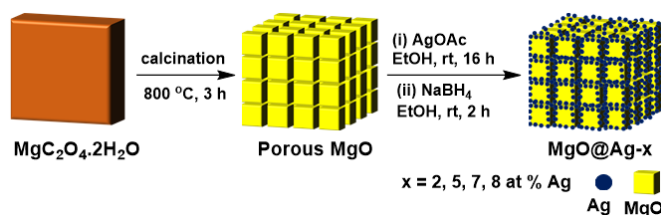


Figure 1. Synthesis of MgO@Ag hybrid nanocatalysts. Schematic illustration for the formation of porous MgO cube host with silver satellite guest.

The internal morphology of microtome sliced MgO@Ag-x hybrid materials reveals the gradual decrease in average size (20 to 5 nm) and increase in the density of Ag NPs with increasing Ag loadings from 2 to 8 at% (Figure S4). The high-resolution SEM and EDX elemental mapping images of MgO@Ag-7, a single hybrid cube, shows the layered structure of MgO embedded with Ag (Figure 2a-e). Furthermore, the STEM-EDX elemental mapping analysis of microtome slices confirms the presence of Ag nanoparticles within the porous MgO cubes (Figure 2f-j). The magnified images reveal the self-assembled structure of nanosized (~100 nm edge length) MgO cubes decorated with (~10 nm) Ag⁰ nanoparticles (Figures 2k-o).

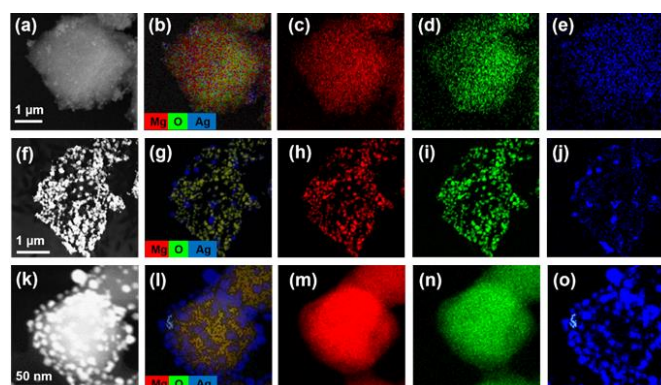


Figure 2. Morphology and elemental mapping of MgO@Ag-7 hybrid cubes. SEM-EDX mapping images (a-e). STEM-EDX mapping images of ultra-microtome sliced cross-section (f-j), and its high magnification view (k-o).

MgO@Ag crystal structure and composition. The crystal structure of MgO@Ag-x (x = 2, 5, 7, 8) hybrid materials is characterized by powder XRD as shown in Figure 3a-d. The phases (111), (200), (220), (311), (222) with corresponding diffraction angles (2θ) at 36.9, 42.9, 62.2, 74.6, 78.5°, respectively, represent pure fcc MgO (Figure S5a, JCPDS no. 4-829). The phases (111), (200), (220), (311) with diffraction angles (2θ) at 38.14, 44.32, 64.53, 77.51°, respectively, denote the pure fcc structure of Ag⁰ nanoparticles and absence of Ag⁺ dopant or oxide (Ag₂O and AgO) impurities (Figure S5b-d, JCPDS card no. 04-0783). A systematic increment in intensity of Ag⁰ peaks w.r.t. MgO peaks was observed with increasing concentrations of Ag⁰ in the MgO@Ag-x (x = 2, 5, 7, 8) hybrid materials, indicating the formation of Ag⁰ nanoparticles in significant concentration (Figure 3a-d).

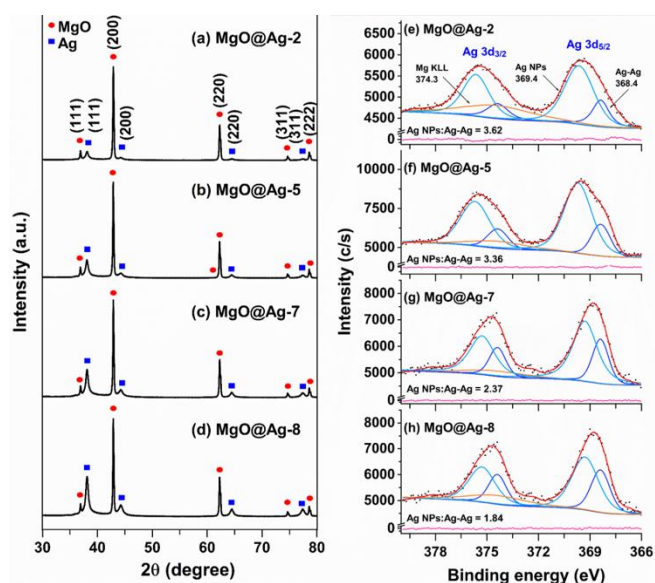


Figure 3. Crystal structure and elemental oxidation state of MgO@Ag-*x*. PXRD and high-resolution core level XPS of Ag3d region for MgO@Ag-2 (a, e), MgO@Ag-5 (b, f), MgO@Ag-7 (c, g) and MgO@Ag-8 (d, h).

The XPS survey spectra of MgO@Ag-*x* hybrid materials also display a similar trend in the intensities of the Ag3d peaks upon increasing concentration of Ag⁰ nanoparticles (Figure S6). The high resolution XPS spectra of MgO@Ag-*x* hybrid materials in the Ag3d region show Ag3d_{5/2} and Ag3d_{3/2} photoelectron signals (Figure 3e-h), which upon deconvolution, reveal the presence of two peaks corresponding to Ag⁰ nanoparticles (< 10 nm) and bulk Ag⁰ aggregate at 369.4, 375.4 eV and 368.4, 374.4 eV, respectively.²⁸ The peak with a binding energy of 374.3 eV in the Ag3d region corresponds to MgKLL photoelectrons (Figure S7).

Gaussian fitting and integration quantify the Ag nanoparticle:Ag aggregate ratio, which decreases from 3.62 (MgO@Ag-2) to 1.84 (MgO@Ag-8) upon increasing the Ag⁰ loading. This suggests a decrease in agglomeration of Ag⁰ nanoparticles, which is in good agreement with TEM images of MgO@Ag-*x* hybrid materials (Figure S4). The analysis of high resolution XPS spectra in the Mg2p and O1s regions show the presence of two types of photoelectrons corresponding to Mg-O (lattice oxides) and Mg-OH (surface hydroxyl groups) with binding energy 50.9 (Mg2p), 531.7 (O1s) eV and 49.7 (Mg2p), 533.7 (O1s) eV, respectively (Figure S8).^{29, 30} The ratio of Mg2p and Ag3d XPS peak areas identifies the at% of surface Ag⁰ as 2, 5, 7 and 8%. These values are compared with bulk elemental composition determination by ICP-MS (1, 3, 4, 5 at% of Ag, respectively). The lower Ag⁰ (at %) values measured by ICP-MS indicate that surface Ag⁰ stabilization is significantly greater than Ag⁰ content deep within the porous MgO cubes. This is consistent with SEM/TEM images of FIB/microtome slices showing reduced Ag⁰ particles deep within the cubes.

The specific surface area and pore volume of the MgO@Ag hybrid catalysts and MgO were analyzed by N₂ adsorption-desorption isotherms (Figure S9, inset Table). The specific surface

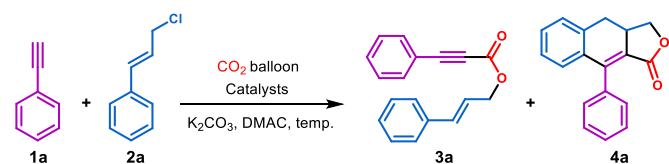
area of 3D MgO cubes is 15.5 m²/g with an average pore size of 33.2 nm and pore volume of 0.13 cm³/g. A slight increase in the BET surface area (18.2, 21.3, 22.0, 22.6 m²/g) with increasing pore size (43.3 to 56.6 nm) and pore volume (0.19 to 0.29 cm³/g) was observed upon increasing Ag loadings (2, 5, 7, 8 at%) within the hybrid catalysts.³¹ The slight modifications in internal morphologies and gradual decrease in average size of Ag NPs (20 to 5 nm) are responsible for the increased BET surface area values (Figure S4).

The strength of the Lewis basic sites within MgO and MgO@Ag hybrid catalysts were measured by temperature programmed desorption (TPD)-CO₂ (Figure S10, Table S2). The moderate (380 °C, 0.32 mmol/g CO₂) and strong (750 °C, 0.1 mmol/g CO₂) Lewis basic sites observed for 3D porous MgO can be attributed to the presence of lattice oxide (Mg²⁺, O²⁻ pairs) and isolated O²⁻ species, respectively.^{26, 32-35} The strength of Lewis basic sites increases with increasing Ag loadings, as evidenced by a shift to higher temperature of the desorption feature and an increase in the peak area (0.65, 1.27, 2.64, 2.7, 2.70 mmol/g of CO₂). This trend highlights the significance of Ag⁰ sites for improving CO₂ chemisorption due to an increased Lewis basic strength of the hybrid catalysts (MgO@Ag-8 > MgO@Ag-7 > MgO@Ag-5 > MgO@Ag-2 > MgO).

CO₂ insertion in alkynes to afford esters and lactones. We have chosen the MgO@Ag-*x* hybrid nanocatalyst to perform the carboxylation of terminal alkynes with CO₂ at 1 atm pressure. The subsequent S_N2 coupling of the carboxylate with allylic chlorides in a tandem manner at the heterogeneous MgO@Ag-*x* interface affords ester and lactone products in good-to-excellent yields. In order to optimize catalyst composition, phenylacetylene (**1a**), cinnamyl chloride (**2a**) and CO₂ (1 atm) were reacted over the MgO@Ag-*x* hybrid catalysts in the presence of K₂CO₃ base and DMAC solvent for 24 h at 55 °C (Table 1). The crude reaction mixtures were purified by column chromatography and initially characterized by ¹H and ¹³C NMR. The ¹H NMR analyses of the ester show three characteristic features, two for the olefinic protons at δ~ 6.34 (dt) and 6.74 (d) ppm and one for (O-CH₂) at δ~ 4.90 (dd) ppm (Figure S12). The ¹³C NMR reveals the characteristic C=O functional group at ~ 153.84 ppm along with two C_{sp} of alkyne at δ~ 86.63 and 80.47 ppm. Also, the allylic (O-CH₂) carbon is observed at δ~ 66.55 ppm (Figure S13). Reaction product analyses demonstrate that the hybrid catalyst with high Ag⁰ loadings (MgO@Ag-7 and MgO@Ag-8) are most efficient, affording ester (**3a**) in 90% yield. At lower Ag⁰ loadings (MgO@Ag-5 and MgO@Ag-2), the yield of **3a** decreases by ~30% for subsequent lower loadings (**3a**: 58 and 29%, respectively). Control experiments using specific catalyst components and alternative formulations (Ag NPs, AgI, MgO or a physical mixture of Ag NPs and MgO) were performed to evaluate the intrinsic species required for effective catalysis (Table 1, Entries 5-8). For Ag NPs (45%) and AgI (30%) catalysts, the formation of CO₂ inserted ester **3a** occurs but the reaction is significantly less efficient than for the MgO@Ag-*x* (*x* = 7 and 8) (90%) due to agglomeration or precipitation of Ag species. This decreases CO₂ adsorption and permits the background formation of the symmetric carbonate side product (~35% yield). In contrast, porous MgO alone produces only the symmetric carbonate side product, indicating that MgO is not suitable for alkyne activation and hence plays a role

in adsorption of CO₂ by Lewis basic sites (moderate to strong) of the porous structure (**Table 1, Entry 7**). Importantly, the physical mixture of Ag NPs and porous MgO generate the ester product in 71% yield with no side product formation, suggesting a synergistic relationship for both metal components in the reaction (**Table 1, Entry 8**).

Table 1. MgO@Ag hybrid catalyzed CO₂ insertion in alkynes to afford esters and lactones.^a



| Entry | Catalyst | Temp. (°C) | Time (h) | Isolated Yield (%) | |
|-------------------|--------------|------------|----------|---------------------|-----------------------|
| | | | | Ester (3a) | Lactone (4a) |
| 1 | MgO@Ag-2 | 55 | 24 | 29 | - |
| 2 | MgO@Ag-5 | 55 | 24 | 58 | - |
| 3 | MgO@Ag-7 | 55 | 24 | 90 | - |
| 4 | MgO@Ag-8 | 55 | 24 | 90 | - |
| 5 ^{b,c} | Ag NPs | 55 | 24 | 45 | - |
| 6 ^{c,d} | AgI | 55 | 24 | 30 | - |
| 7 ^{c,e} | MgO | 55 | 24 | - | - |
| 8 ^f | Ag NPs + MgO | 55 | 24 | 71 | - |
| 9 | MgO@Ag-7 | RT | 48 | - | - |
| 10 | MgO@Ag-7 | 70 | 18 | 52 | 35 |
| 11 | MgO@Ag-7 | 90 | 12 | - | 90 |
| 12 ^g | MgO@Ag-7 | 55 | 24 | 90 | - |
| 13 ^h | MgO@Ag-7 | 55 | 24 | 80 | - |
| 14 ⁱ | MgO@Ag-7 | 55 | 24 | 60 | - |
| 15 ^{c,j} | MgO@Ag-7 | 55 | 48 | - | - |

^aReaction conditions: phenylacetylene **1a** (1.0 mmol), cinnamyl chloride **2a** (1.0 mmol) and catalyst (6 mg), DMAC (0.5 mL), K₂CO₃ (1.2 mmol), CO₂ balloon. ^bUltra-small (5 nm) Ag NPs quantity 1 mg is equivalent to MgO@Ag-7 (15 wt% Ag). ^cSymmetric carbonate side product is formed. ^dReaction was performed with 0.1 mol% of AgI (1 mg Ag⁺). ^ePorous MgO (5 mg). ^fUltra-small Ag NPs (1 mg) + porous MgO (5 mg). ^gCS₂CO₃ is used as a base. ^h50% of CO₂ with N₂ mixture (0.5 + 0.5 atm). ⁱ25% of CO₂ with N₂ mixture (0.25 + 0.75 atm). ^jWithout CO₂.

To evaluate the role of temperature and time on the MgO@Ag-7 catalyzed synthesis of **3a** and **4a**, control reactions were performed at ambient (48 h) and elevated temperatures (70, 90 °C) for 18 and 12 h (**Table 1, Entries 9-11**). Under ambient conditions, no product formation is observed, indicating the formation of **3a** is endergonically controlled. When the reaction is performed above the optimized formation temperature of 55 °C (e.g. 70 °C), partial dehydro-Diels-Alder (DDA) cyclo-isomerization of **3a** to lactone **4a** is observed (35%). At 90 °C, the reaction proceeds completely to lactone **4a** without detection of the ester precursor, consistent with the acatalytic nature of the cyclo-isomerization step. The effect of strong base (CS₂CO₃) on the progress of the reaction was also screened under optimized conditions, and found to contribute no further improvement in the yield (90%) of ester **3a** (**Table 1, Entry**

12). For reactions performed at 1 atm total pressure under N₂-diluted CO₂ concentrations of 0.5 and 0.25 atm, the results reveal a drop in the yield of ester **3a** to 80 and 60%, respectively (**Table 1, Entries 13 and 14**). In order to understand the binding affinity of the MgO@Ag-7 catalyst for CO₂, a Michaelis-Menten curve³⁶⁻³⁸ was fit for the formation of ester **3a** as a function of CO₂ concentration and compared to data reported for the CeO₂@Ag catalyst.²³ The low Michaelis-Menten constant (K_M = 2.95 vs. 8.8 mM) for MgO@Ag-7 and comparable reaction velocity (V_{max} = 45.19 vs. 41.03 mM/hr) indicate higher CO₂ binding affinity for MgO@Ag-7 than CeO₂@Ag (**Figure S11, Table S3**). This is also reflected in comparable product yields for these two catalysts even when markedly reduced CO₂ concentration is employed over MgO@Ag-7 (5:1 atm CO₂). Finally, in the absence of externally introduced CO₂, MgO@Ag-7 shows no ester formation and only symmetric carbonate side product even at prolonged reaction times, demonstrating that incorporated CO₂ does not derive from the K₂CO₃ base (**Table 1, Entry 15**).

The efficiencies of MgO@Ag-7 and CeO₂@Ag for the synthesis of ester **3a** from the reaction of phenylacetylene, CO₂ and cinnamyl chloride under identical conditions were directly compared (**Table S4**).²³ The results reveal a five-fold higher turnover frequency (TOF) at 1 atm CO₂ for MgO@Ag-7 and comparable activity even at low concentrations of CO₂ (0.25 atm). Moreover, MgO@Ag-7 exhibits 2-7 folds higher turnover frequency for the synthesis of phenylpropionic acid compared to the reported Ag⁰-stabilized MgO and MOF based heterogeneous catalysts (**Table S5**).^{20, 24, 39, 40} The higher catalytic activity of the MgO@Ag-7 hybrid catalyst over these examples must derive from the synergy of Ag⁰ and 3D porous MgO for improving Lewis basicity and the local concentration of CO₂.

Scope for substituted ester and lactone products. The optimized reaction conditions were used to demonstrate the wide substrate scope for the MgO@Ag-7 catalyzed synthesis of CO₂-inserted esters and cyclo-isomerized lactones. Reaction of various substituted aromatic terminal alkynes (**1**) bearing electron-donating (4-Me, 3-Me, 4-^tBu, 4-OMe, 3-OMe) or electron-withdrawing (4-F, 4-CN) groups with various allylic and other chloride (cinnamyl chloride **2a**, 3-chloro-1-phenyl-1-propyne **2b**, ethyl 2-chloroacetate **2c** and benzyl chloride **2d**) substrates gives the corresponding esters **3a-3p** (55 °C, 24 h) and lactones **4a-5c** (90 °C, 12 h) as shown in **Table 2 (Figures S12-S65)**. For phenylacetylene or derivatives bearing electron donating groups, the reaction with allylic chlorides generates the corresponding ester products in very good yields (78-83%). The conversion is only modestly affected by electron withdrawing functional groups as 4-F-phenylacetylene gives the desired ester products in 68-84% yields. For reaction of 4-CN-phenylacetylene with cinnamyl chloride, the lactone product is the only species detected both at 55 and 90 °C, due to the facile cyclization of the ester caused by decrease in energy of the dienophile LUMO. For all reactions at 90 °C, spontaneous DDA cyclization of the ester occurs to form the corresponding lactone products in 61-95% yields. While the cinnamyl chloride reactions form single isomer dihydrolactone heterocycles (**4**),⁴¹ the esters formed by coupling of phenylacetylenes **1** and 3-chloro-1-phenyl-1-propyne **2b**, furnish a

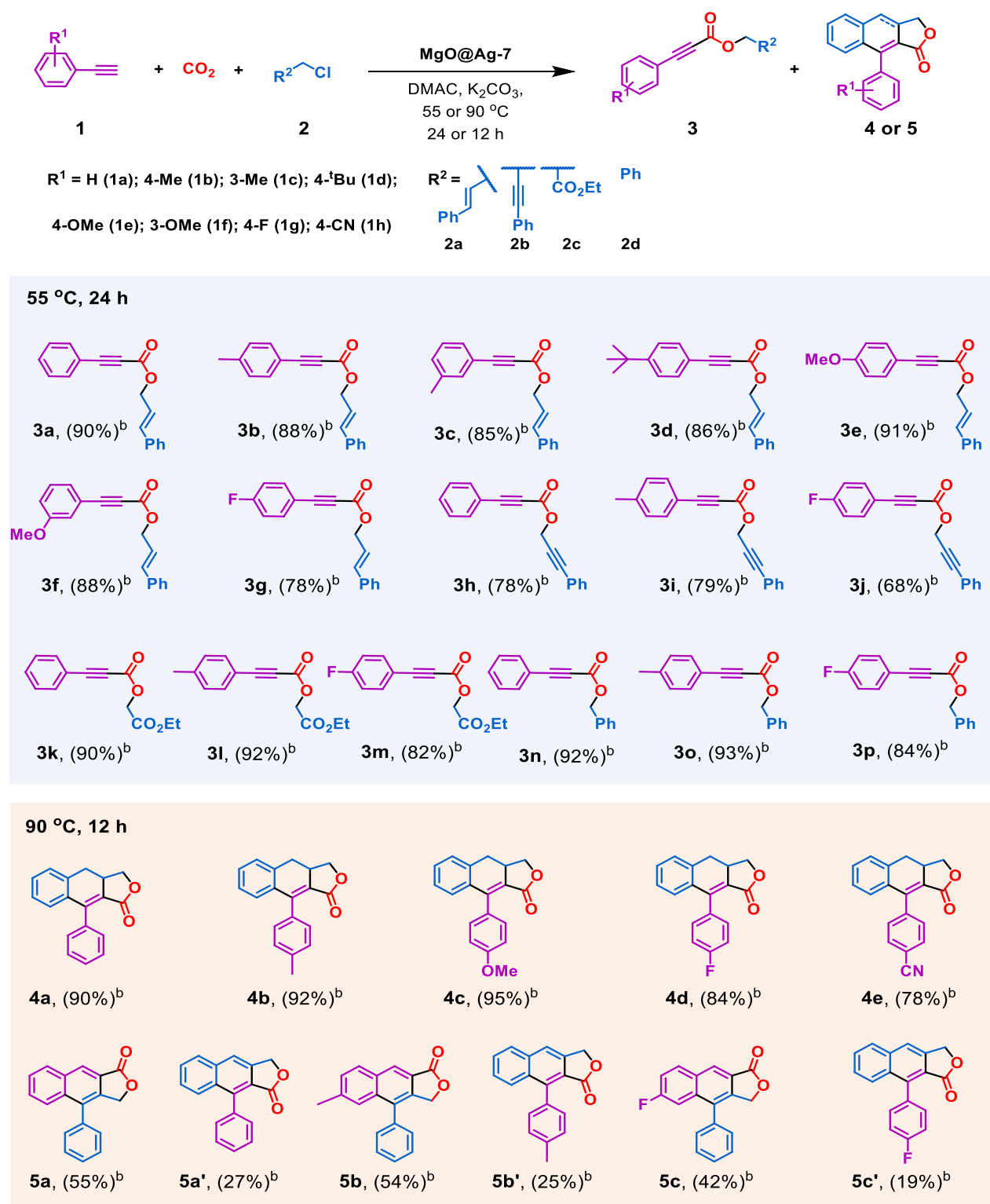
Journal Name

ARTICLE

mixture of major (**5**) and minor (**5'**) lactones as separable regioisomers.⁴¹ There is also a significant decrease in yield (~8-23%) for lactone (vs. dihydrolactone) formation due to the higher distortion energy for the diyne (vs. enyne) ester during the DDA cyclization step.⁴²

ambient pressure incorporation of CO₂ into electron rich alkynes for the formation of esters at the MgO@Ag-x hybrid catalysts (Figure

Table 2. MgO@Ag-7 catalysed CO₂ insertion in alkyne substrates to afford esters and lactones.^a



^aReaction conditions: The mixture of alkynes **1** (1 mmol), allylic chlorides **2** (1 mmol) and MgO@Ag-7 catalyst (6 mg), K₂CO₃ (1.2 mmol) in DMAC (0.5 mL), CO₂ balloon at 55 °C, 24 h. ^bIsolated yields.

MgO@Ag-x hybrid nanocatalyst mechanism. Combining these observations leads to a reasonable mechanistic proposal for **4**). Control experiments reveal that alkyne activation and CO₂ incorporation are predominantly occurring at Ag⁰ sites (Table 1),

however their aggregation lowers the reaction efficiency as observed by competition from symmetric carbonate side product formation. The porous MgO 3D framework prevents the aggregation of Ag⁰ nanoparticles and enhances the local concentrations of CO₂ and alkyne substrates. Moreover, Lewis acidic Mg²⁺ activates the C-Cl bond of alkyl chlorides to trigger the S_N2 reaction. Therefore, the proximity of MgO and Ag⁰ sites in the MgO@Ag-x hybrid catalyst prompts their synergy in catalyzing the synthesis of CO₂ inserted esters **3**.

Initially, activation of alkyne **1** at Ag⁰ via deprotonation with K₂CO₃ base (**A**) leads to the terminal acetylide (**B**). The Ag⁰, assisted by Lewis basic lattice oxides of MgO, adsorb and insert CO₂ in C_{sp}-Ag⁰ bond (**C**) at 1 atm pressure to afford the phenylpropiolate intermediate (**D**). The Lewis acidic Mg²⁺ activates the C-Cl bond of alkyl chloride **2** and carbonyl oxygen of intermediate **D** triggering S_N2 substitution to form the desired ester product (**3**). At high temperature, the esters (**3a-3j**) formed by S_N2 coupling with cinnamyl chloride **2a** and 3-chloro-1-phenyl-1-propyne **2b**, spontaneously undergo dehydro-Diels-Alder cyclo-isomerization⁴³ to the dihydro-lactone (**4**) and lactone (**5**) heterocycles, respectively, independent of catalyst.

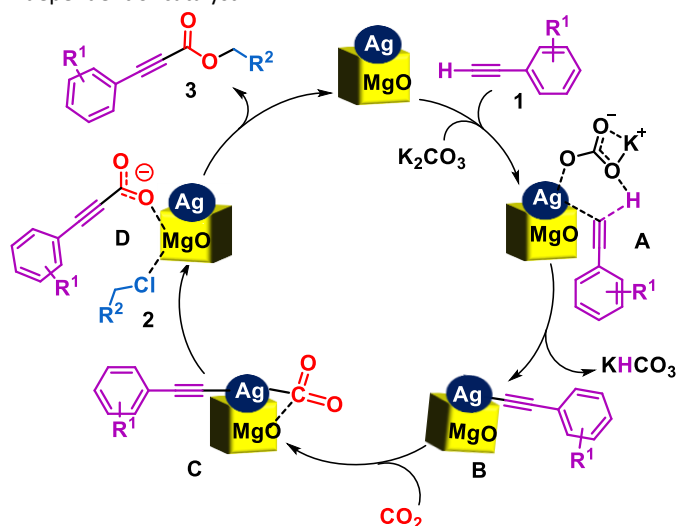


Figure 4. Proposed mechanism for MgO@Ag-x hybrid cubes catalysis. The CO₃²⁻ base triggered C(sp)-H activation of alkyne (**1a**) leads to formation of intermediate (**A**). Deprotonation of the alkyne in intermediate (**A**) leads to the Ag-acetylide intermediate (**B**). The basic lattice oxides of MgO and Ag(0) nanoparticles promote CO₂ adsorption/insertion into the Ag-acetylide bond (**C**) leading to the phenylpropiolate-Ag intermediate (**D**). S_N2 reaction of phenylpropiolate on Mg-activated cinnamyl chloride (**2a**) in intermediate (**D**) generates ester intermediate **3a**.

Recyclability and structural integrity of MgO@Ag-7 hybrid nanocatalyst. The recyclability of the MgO@Ag-7 hybrid nanocatalyst was studied for five consecutive cycles using a model reaction of phenylacetylene (**1a**), CO₂ and cinnamyl chloride (**2a**) on the 5 mmol scale under optimized reaction conditions (**Figure 5**). The results show excellent recyclability without significant decrease in catalytic efficiency (85%) over five cycles (**Figure 5A**). The blemish in yield can be attributed to minor catalyst restructuring. The PXRD of the recovered MgO@Ag-7 catalyst (five cycles) shows an increase

in intensity of the Ag⁰ diffraction peaks w.r.t. to those from MgO due to very slow agglomeration of Ag⁰ nanoparticles (**Figure 5B**). The surface morphology of recovered MgO@Ag-7 also exhibits a gradual formation of detectable Ag⁰ aggregates and erosion of ~10% of the number of MgO cubes after the fifth cycle (**Figure 5C**). The high-resolution XPS of the Ag3d region supports the slow aggregation of Ag⁰ nanoparticles during recycling with a decrease in Ag nanoparticles:Ag aggregate ratio from 2.37 to 0.71 in recovered vs fresh nanocatalyst (**Figure 5D**). Taken together, these results suggest that while Ag aggregation and modest MgO dissolution occur, these processes are slow and do not markedly affect the performance of the hybrid catalyst.

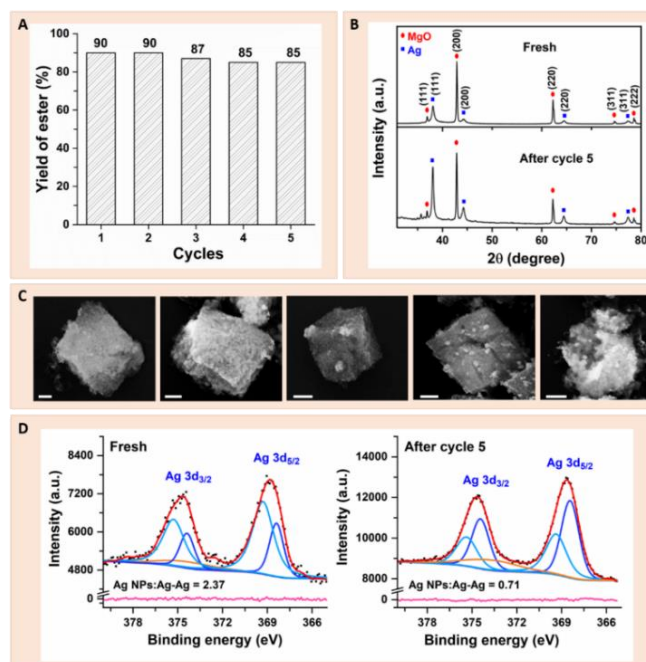


Figure 5. Recyclability of MgO@Ag-7 hybrid catalyst. **A.** Comparing yield of ester (**3a**) for five subsequent cycles **B.** PXRD of fresh and recovered catalyst after five cycles **C.** SEM images of recovered catalyst after first to fifth cycle. All scale bars are 500 nm **D.** High resolution XPS of Ag 3d region for fresh and recovered catalyst after five cycles.

Green chemistry E-factor of MgO@Ag-7 hybrid nanocatalyst.

The development of chemical processes feasible at ambient temperature and pressure comes under the twelve principles of green chemistry.⁷ Previous reports of CO₂ insertion in aromatic terminal alkynes followed by S_N2 coupling with cinnamyl chloride using homogeneous (1.5 MPa) and heterogeneous (0.5 MPa) catalysts require high pressures of CO₂ to drive high yields (~90%).^{15, 17, 23} Also, these reactions require excess equivalents of substrates and base in relatively large amounts of high boiling solvent, which are not readily recoverable after the reaction. Thus, these transformations have high waste-to-product ratios (E-factor ~ 21 to 41) per reaction cycle. In contrast, the MgO@Ag-x hybrid nanocatalyst performs the unprecedented insertion of CO₂ into unsaturated substrates with comparable yields at 1 atm pressure. Moreover, the E-factor for the present catalyst system (2.8) is an order of magnitude (7 to 14 fold) lower than those of other

reported methods (Table S1) since these conditions avoid excess equivalents of substrates, base, and solvent.^{15, 17, 23}

Conclusions

We have developed a three dimensional (3D) porous MgO framework embedded with Ag⁰ nanoparticles (MgO@Ag-x = 2, 5, 7, 8%) as a Lewis base-noble metal hybrid catalyst. The porous structure allows the uniform growth of Ag⁰ nanoparticles on surface as well as within the pores of MgO cubes. These hybrid nanocatalyst are found to be highly efficient for activating and inserting CO₂ in alkynes at ambient pressure for synthesis of a wide array of esters and lactone heterocycles. The synergy of both metal components for alkyne activation (Ag⁰), CO₂ incorporation (Ag⁰) and high accessibility (MgO) are responsible for its high catalytic efficiency. The hybrid nanocatalyst performs well over five catalytic cycles with no significant loss in yield of the ester product. The feasibility of the CO₂ insertion reaction at 1 atm pressure with higher TOF (4.7 h⁻¹) and low E-factor (2.8) of the present catalytic system is an order of magnitude (5 to 14-folds) better than reported methods making it a substantially green approach. Finally, the MgO@Ag-x hybrid nanocatalyst demonstrates the unique combination of efficient synergistic catalysis and green methodology for transformation of CO₂ feedstock to valuable organic molecules.

Conflicts of interest

The authors declare no competing financial interests.

Acknowledgements

J.M.Z acknowledge the financial support of the National Science Foundation (CHE-1265703) and the National Institutes of Health (NIH5R01). D.S.R. thanks Council of Scientific and Industrial Research (CSIR), India (File Number: 02(0318)/17/EMR-II) for financial support. U.G. acknowledges DU (DRC/BRS committee) and CSIR for the exchange visiting opportunity and the award of Junior/Senior Research Fellowship, respectively. The authors thank Dr. Barry Stein, Dr. David Gene Morgan (Electron Microscopy Center) and Dr. Yaroslav Losovyj (Molecular Structure Center) for their help with ultra-microtome, HR-TEM/STEM and XPS data collection of the materials, respectively. The authors thank Dr. Shelby Rader (The Metal Isotopes Laboratory, Department of Earth and Atmospheric Sciences) for ICP-MS analysis.

Notes and references

1. D. U. Nielsen; X.-M. Hu; K. Daasbjerg; T. Skrydstrup, *Nat. Catal.*, 2018, **1**, 244-254.
2. S. C. Peter, *ACS Energy Lett.*, 2018, **3**, 1557-1561.
3. J. Wei; Q. Ge; R. Yao; Z. Wen; C. Fang; L. Guo; H. Xu; J. Sun, *Nat. Commun.*, 2017, **8**, 15174.
4. M. Poliakoff; W. Leitner; E. S. Streng, *Faraday Discuss.*, 2015, **183**, 9-17.

5. M. Aresta; I. Tommasi, *Energ. Convers. Manag.*, 1997, **38**, S373-S378.
6. J. H. Clark, *Green Chem.*, 2006, **8**, 17-21.
7. J. H. Clark, *Green Chem.*, 1999, **1**, 1-8.
8. R. A. Sheldon, *Green Chem.*, 2007, **9**, 1273-1283.
9. R. A. Sheldon, *Green Chem.*, 2016, **18**, 3180-3183.
10. D. C. Graham; C. Mitchell; M. I. Bruce; G. F. Metha; J. H. Bowie; M. A. Buntine, *Organometallics*, 2007, **26**, 6784-6792.
11. H. Hoberg; K. Jenni; K. Angermund; C. Krüger, *Angew. Chem. Int. Ed.*, 1987, **26**, 153-155.
12. N. Huguet; I. Jevtovikj; A. Gordillo; M. L. Lejkowski; R. Lindner; M. Bru; A. Y. Khalimon; F. Rominger; S. A. Schunk; P. Hofmann; M. Limbach, *Chem. Eur. J.*, 2014, **20**, 16858-16862.
13. C. S. Yeung; V. M. Dong, *J. Am. Chem. Soc.*, 2008, **130**, 7826-7827.
14. B. Yu; Z.-F. Diao; C.-X. Guo; L.-N. He, *J. CO₂ Util.*, 2013, **1**, 60-68.
15. W.-Z. Zhang; W.-J. Li; X. Zhang; H. Zhou; X.-B. Lu, *Org. Lett.*, 2010, **12**, 4748-4751.
16. X. Zhang; W.-Z. Zhang; X. Ren; L.-L. Zhang; X.-B. Lu, *Org. Lett.*, 2011, **13**, 2402-2405.
17. X. Zhang; W.-Z. Zhang; L.-L. Shi; C. Zhu; J.-L. Jiang; X.-B. Lu, *Tetrahedron*, 2012, **68**, 9085-9089.
18. F. Manjolinho; M. Arndt; K. Gooßen; L. J. Gooßen, *ACS Catal.*, 2012, **2**, 2014-2021.
19. P. Bhanja; A. Modak; A. Bhaumik, *Chem. Eur. J.*, 2018, **24**, 7278-7297.
20. X.-H. Liu; J.-G. Ma; Z. Niu; G.-M. Yang; P. Cheng, *Angew. Chem. Int. Ed.*, 2015, **54**, 988-991.
21. Y. Ma; Z. Wang; X. Xu; J. Wang, *Chinese J. Catal.*, 2017, **38**, 1956-1969.
22. R. A. Molla; K. Ghosh; B. Banerjee; M. A. Iqbal; S. K. Kundu; S. M. Islam; A. Bhaumik, *J. Colloid Interf. Sci.*, 2016, **477**, 220-229.
23. X. Zhang; D. Wang; M. Jing; J. Liu; Z. Zhao; G. Xu; W. Song; Y. Wei; Y. Sun, *ChemCatChem*, 2019, **11**, 2089-2098.
24. J. Shi; L. Zhang; N. Sun; D. Hu; Q. Shen; F. Mao; Q. Gao; W. Wei, *ACS Appl. Mater. Inter.*, 2019, **11**, 28858-28867.
25. D. Yu; M. X. Tan; Y. Zhang, *Adv. Synth. Catal.*, 2012, **354**, 969-974.
26. G. A. Mutch; S. Shulda; A. J. McCue; M. J. Menart; C. V. Ciobanu; C. Ngo; J. A. Anderson; R. M. Richards; D. Vega-Maza, *J. Am. Chem. Soc.*, 2018, **140**, 4736-4742.
27. C. Liang; W. Xiao; H. Hao; L. Xiaoping; L. Chao; Z. Lei; H. Fashui, *Biol. Trace Elem. Res.*, 2008, **121**, 249-257.
28. S. Calderon V; R. E. Galindo; N. Benito; C. Palacio; A. Cavaleiro; S. Carvalho, *J. Phys. D: Appl. Phys.*, 2013, **46**, 325303.
29. S. Benedetti; N. Nilius; P. Torelli; G. Renaud; H. J. Freund; S. Valeri, *J. Phys. Chem. C*, 2011, **115**, 23043-23049.
30. S. Wuttke; S. M. Coman; G. Scholz; H. Kirmse; A. Vimont; M. Daturj; S. L. M. Schroeder; E. Kemnitz, *Chem. Eur. J.*, 2008, **14**, 11488-11499.
31. X. Jiang; H. Liu; H. Liang; G. Jiang; J. Huang; Y. Hong; D. Huang; Q. Li; D. Sun, *Ind. Eng. Chem. Res.*, 2014, **53**, 19128-19135.
32. J. Hu; K. Zhu; L. Chen; C. Kübel; R. Richards, *J. Phys. Chem. C*, 2007, **111**, 12038-12044.
33. K. Sasaki; N. Fukumoto; S. Moriyama; T. Hirajima, *J. Hazard. Mater.*, 2011, **191**, 240-8.
34. Y. Yanagisawa; K. Takaoka; S. Yamabe; T. Ito, *J. Phys. Chem.*, 1995, **99**, 3704-3710.
35. Y. Zheng; X. Zhang; Z. Bai; Z. Zhang, *Rapid Commun. Mass Spectrom.*, 2016, **30**, 217-225.

36. F. Li; N. Li; C. Xue; H. Wang; Q. Chang; H. Liu; J. Yang; S. Hu, *Chem. Eng. J.*, 2020, **382**, 122484.
37. N. Lu; M. Zhang; L. Ding; J. Zheng; C. Zeng; Y. Wen; G. Liu; A. Aldalbahi; J. Shi; S. Song; X. Zuo; L. Wang, *Nanoscale*, 2017, **9**, 4508-4515.
38. P. C. Pandey; S. Singh; A. Walcarius, *J. Electroanal. Chem.*, 2018, **823**, 747-754.
39. A. H. Chowdhury; S. Ghosh; S. M. Islam, *New J. Chem.*, 2018, **42**, 14194-14202.
40. N. N. Zhu; X. H. Liu; T. Li; J. G. Ma; P. Cheng; G. M. Yang, *Inorg. chem.*, 2017, **56**, 3414-3420.
41. N. Eghbali; J. Eddy; P. T. Anastas, *J. Org. Chem.*, 2008, **73**, 6932-6935.
42. P. Yu; Z. Yang; Y. Liang; X. Hong; Y. Li; K. N. Houk, *J. Am. Chem. Soc.*, 2016, **138**, 8247-8252.
43. P. Wessig; G. Müller, *Chem. Rev.*, 2008, **108**, 2051-2063.

Table of Contents (TOC) graphic

Development of Magnesium Oxide-Silver Hybrid Nanocatalysts for Synergistic Carbon Dioxide Activation to Afford Esters and Heterocycles at Ambient Pressure